

UKAEA-CCFE-PR(23)177

P. J. Ryan S. D. Elmore J. R. Harrison J. Lovell R.  
Stephen

# Overview of the MAST Upgrade Langmuir Probe System

Enquiries about copyright and reproduction should in the first instance be addressed to the UKAEA Publications Officer, Culham Science Centre, Building K1/O/83 Abingdon, Oxfordshire, OX14 3DB, UK. The United Kingdom Atomic Energy Authority is the copyright holder.

The contents of this document and all other UKAEA Preprints, Reports and Conference Papers are available to view online free at [scientific-publications.ukaea.uk/](https://scientific-publications.ukaea.uk/)

# **Overview of the MAST Upgrade Langmuir Probe System**

P. J. Ryan S. D. Elmore J. R. Harrison J. Lovell R. Stephen



# Overview of the Langmuir Probe System on the Mega Ampere Spherical Tokamak (MAST) Upgrade

P. J. Ryan,<sup>1, a)</sup> S. D. Elmore,<sup>1</sup> J. R. Harrison,<sup>1</sup> J. Lovell,<sup>2</sup> and R. Stephen<sup>1</sup>

<sup>1)</sup>United Kingdom Atomic Energy Authority, Culham Centre for Fusion Energy, Culham Science Centre, Abingdon, Oxon, OX14 3DB, U.K

<sup>2)</sup>Oak Ridge National Laboratory, Oak Ridge, Tennessee 37831, USA

(Dated: 7 September 2023)

A detailed description of the Langmuir probe system on MAST Upgrade is presented. The system features 850 tile embedded probes, and 40 bespoke electronic modules which each have the capability to drive and acquire data from up to 16 probes in a time multiplexed manner. The system provides spatio-temporal resolved measurements (1 cm and  $\sim 1$  ms respectively) in the divertor region of ion saturation current, electron temperature and floating potential. The standard interpretation of current-voltage ( $IV$ ) characteristics is to apply a 4 parameter fit, based on unmagnetized probe theory, which includes a linear model for the ion saturation region. To mitigate the effect of the magnetic field, analysis is restricted to the region of the  $IV$  characteristic that is sensitive to only the tail of the electron energy distribution function.

## I. INTRODUCTION

MAST Upgrade was designed to explore the comparative benefits of conventional and alternative configurations, in particular the Super-X configuration<sup>1</sup> with tightly baffled divertor chambers. The Langmuir probe system on MAST-U, which features 850 tile embedded probes, provides spatio-temporal resolved measurements (1 cm and  $\sim 1$  ms respectively) of important plasma parameters for assessing the divertor conditions; namely ion density ( $n_i$ ), electron temperature ( $T_e$ ), floating potential ( $V_f$ ) and tile heat flux ( $q_{\perp tile}$ ). The main advantage of Langmuir probe diagnostics compared to divertor Thomson scattering<sup>2</sup>, which provides accurate measurements of electron density and  $T_e$ , is the relatively simple experimental setup which can be repeated for many probes to give excellent spatial coverage around the device. Infrared (IR) thermography is an inherently different technique that also provides spatio-temporal resolved measurements of  $q_{\perp tile}$ , and so measurements from the two diagnostics can be compared to corroborate results.

Standard Langmuir probe operation involves measuring the current collected from the plasma as the electric potential of the probe is varied. A probe theory is used to extract plasma parameters from the current-voltage ( $IV$ ) characteristic. General probe theories for interpreting  $IV$  data from magnetized plasma are challenging to develop because cross-field transport mechanisms and their associated rates, which determine the probe disturbance length<sup>3,4</sup> and return electrode collection area<sup>5</sup>, are device dependent<sup>6</sup>. Common approaches for analysing  $IV$  data from tokamaks<sup>7,8</sup> and stellarators<sup>9</sup> are to apply an asymmetric double probe model<sup>5</sup> to the entire  $IV$  characteristic, or use unmagnetized single probe theory and restrict the upper voltage in the analysis to

$V \lesssim V_f$  to avoid probe voltages that significantly perturb the bulk plasma<sup>10,11</sup>. Non-saturation of the net ion current region is included in the  $IV$  models via an additional fitting parameter<sup>5,12</sup>, a self-consistent Child-Langmuir sheath solution<sup>13</sup> or parameterisation of simulation results<sup>14,15</sup>. The effective ion collection area of the probe ( $A_i$ ) for calculating ion density is usually taken as the projected area of the probe along the magnetic field ( $A_{projected}$ ). The inferred  $T_e$  and ion saturation current density from an  $IV$  characteristic can vary by up to a factor of  $\sim 2$  depending on the analysis procedure and plasma conditions<sup>7-10,12,13</sup>.

The aim of this contribution is to give a comprehensive overview of the MAST-U Langmuir probe system in terms of hardware (section II), probe positions (section III), probe designs (section IV), and the procedure for generating and analysing  $IV$  characteristics (section V) that was implemented during the first and second MAST-U campaigns. In this article  $T_e$  is given in units of electronvolts.

## II. HARDWARE

The Langmuir probe system consists of 850 tile embedded probes and 40 bespoke electronic modules<sup>16,17</sup> which have the capability to drive and acquire data from 640 probes in each shot. A schematic of the system is shown in figure 1. Each electronic module is comprised of a power supply, an amplifier ( $\pm 200$  V,  $\pm 3.5$  A), and a novel FPGA-based multiplexer which controls up to 16 probes via 16 output channels and records the  $IV$  data at 1 Msps. The output voltage from the multiplexer is with respect to the vessel (and tile) electric potential. The patching of probes to multiplexer channels occurs in the marshalling cubicles using BNC terminations on a weekly basis during MAST-U scientific campaigns. The choice of operational probes depends on the scheduled experiments: there should be sufficient poloidal spatial coverage to diagnose the divertor configuration<sup>18</sup>, and

---

<sup>a)</sup>The author to whom correspondence may be addressed: peter.ryan@ukaea.uk

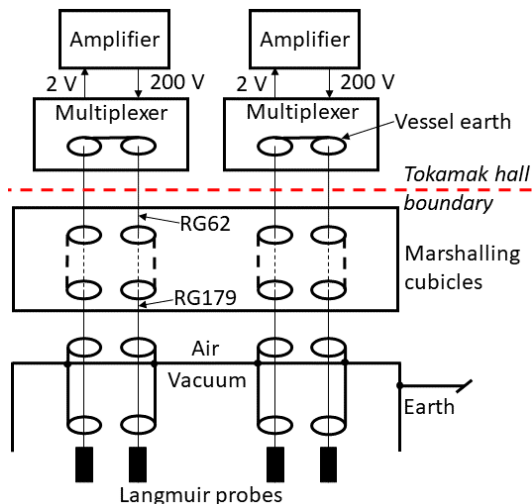


FIG. 1. Schematic of the Langmuir probe system. There are a total of 40 multiplexer units (2 are shown), each multiplexer has 16 outputs (2 are shown), and there are a total of 850 in-vessel Langmuir probes (4 are shown).

toroidal spatial coverage can be requested with the same or different multiplexer settings.

Multiplexer output voltage and channel sequence waveforms are programmable between shots, and each multiplexer can be programmed independently. For the case of 16 active channels with a monotonic channel sequence waveform, the time between consecutive measurements by a specific probe is  $16T_V$ , where  $T_V$  is the time period of the voltage waveform. There are two routine modes of operation:  $I_{sat}^+$  mode and swept mode. In both modes, the applied voltage is set to  $\sim 0$  V before switching channels. This is to mitigate large current transients, due to a sudden change in sheath resistance as the channel is switched, which could damage the amplifier. Ideally the switching voltage would be at the floating potential but these values cannot be predetermined before the shot. The non-driven probes are electrically floating. During each voltage waveform period, a multiplexer can simultaneously measure  $V_f$  from the 15 non-driven probes at 1 Msp. This feature is not used by default to limit data storage.

During  $I_{sat}^+$  mode, a DC voltage (typically  $\leq -150$  V) is applied to the probe to measure fluctuations of the ion saturation current at 1 Msp. Example voltage, current and channel sequence measurements by a multiplexer in  $I_{sat}^+$  mode are shown in figure 2. The voltage waveform period is customised for each experiment ( $T_V$  ranges from 10's  $\mu$ s to 100's ms). The voltage and current slew rates of the electronic module have been measured:  $\sim 110$  V/ $\mu$ s and  $\sim 0.94$  A/ $\mu$ s. Assuming a sinusoidal current waveform with an amplitude of 500 mA, the maximum  $I_{sat}^+$  frequency that can be measured without slew rate limitation is  $\sim 300$  kHz.

Swept mode is used to generate  $IV$  characteristics (typically from -140 V to +20 V) which are analysed

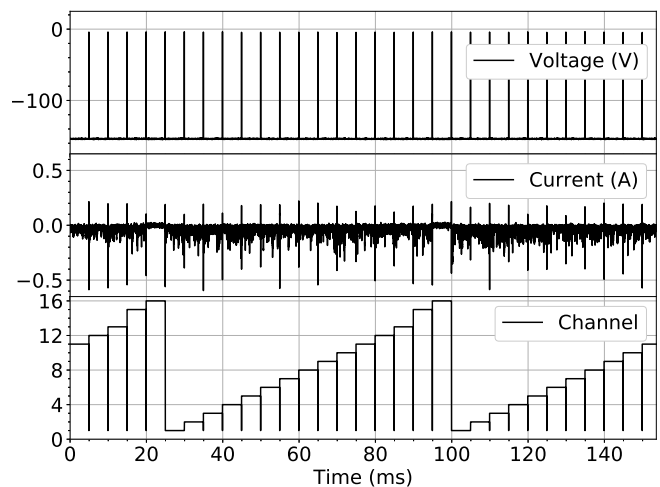


FIG. 2. Example measurements from a multiplexer in  $I_{sat}^+$  mode during a plasma current flattop phase.

to determine  $I_{sat}^+$ ,  $V_f$  and  $T_e$ . Example waveforms are shown in figure 3. The minimum voltage sweep period for a symmetrical waveform is limited to  $T_V \gtrsim 60$   $\mu$ s by the  $\sim 65$  kHz power bandwidth (-3 dB) of the amplifier.

The main advantages of the digital FPGA approach, rather than analog electronics, is the excellent configurability of the system as demonstrated above and the moving of complexity from hardware to software. The latter results in fewer physical points of failure and makes it easier to add new features after the system is deployed. Time multiplexing the probes, rather than having an individual amplifier per probe, greatly reduces the cost, space and peak power requirement of the system. This is essential for operating a large scale system of 640 probes per shot. Standard operation of a multiplexer applies the output voltage to only one probe at any given time, rather than a few probes in parallel, to mitigate the risk of exceeding the maximum current rating of the amplifier.

### III. PROBE POSITIONS

There are a total of 850 tile embedded Langmuir probes installed in MAST-U with coverage of the centre column, divertor target and nose region; upper and lower divertors; and two toroidal locations per probe set (except for the centre column probes) which gives the option of obtaining both swept data and  $I_{sat}^+$  fluctuation data at the same position in the poloidal plane for a given shot. Figure 4 shows the probe positions in the poloidal plane and tile groups are labelled, and table I details the toroidal distribution of the probes and the probe tip design (section IV). The nominal probe spacing is 1 cm in the poloidal plane.

Each group of tiles covers an angular span of  $2\pi$  radians around the torus. The tiles are identical within a

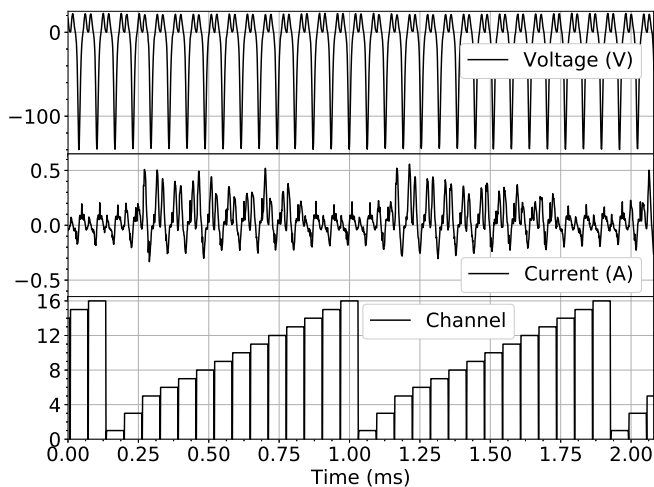


FIG. 3. Example measurements from a multiplexer in swept mode during a plasma current flattop phase.

group except for T5. Four different T5 tiles were produced (named A-D) which were shaped (surface-normal unit vectors denoted by  $\hat{n}_{tile}^R$ ), based on SMARDDA analysis<sup>19</sup>, to compensate for the toroidal field ripple (mode number 12) to ensure toroidally symmetric particle and heat fluxes on T5. For tile T5, effective tile surface-normal unit vectors ( $\hat{n}_{tile}$ ) were used in the analysis for tile related quantities (e.g.  $q_{\perp tile}$ ) which are toroidally symmetric and satisfy:

$$\hat{n}_{tile} \cdot \hat{B}_{EFIT} \approx \hat{n}_{tile}^R \cdot \hat{B}_{3D}, \quad (1)$$

where  $\hat{B}_{EFIT}$  is the toroidally symmetric magnetic field unit vector from the EFIT++ (Equilibrium Fitting) code<sup>20</sup> and  $\hat{B}_{3D}$  is the magnetic field unit vector that includes the toroidal field ripple.

The toroidal field ripple is also significant for T4, but these tiles were not shaped to give toroidally symmetric particle and heat fluxes. The Langmuir probes on T4 and T5 have the same toroidal locations (between T5A and T5D), and measure the same phase of the toroidal field ripple when comparing the two toroidal locations (sectors 4 and 10). A detailed study into asymmetric divertor fluxes due to the toroidal field ripple on MAST-U is beyond the scope of this article.

#### IV. PROBE DESIGNS

There are six different designs of electrode installed in MAST-U. Figures 5 and 6 show the designs and their position relative to the adjacent tiles; dimensions are given in table II. The designs can be split into four groups based on their position inside the tokamak: divertor target tiles (designs 1 and 2), nose tiles (designs 3 and 4), centre column tiles (design 5) and baffle tiles (design 6).

Different probe designs were motivated by variations in the expected heat flux and magnetic field incidence angle for each group.

General design features include: (i) designs 1-5 are non-flush with the adjacent tiles to reduce the impact of sheath expansion<sup>21</sup>, and hence make  $IV$  data interpretation more straightforward; (ii) the probe expands in size below the tile surface to increase the heat capacity of the probe body; (iii) the probe material is pyrolytic graphite for designs 1 and 2, and fine grain graphite for designs 3-6. The divertor target tiles (designs 1 and 2) are expected to receive the greatest heat flux. The pyrolytic graphite has lamellae orientated along the (b) direction (defined in figure 5) and parallel to the tile surface-normal vector to ensure good heat conduction across the probe and through the probe to the mount for dissipation. (iv) The surface  $\hat{n}_{probe}$  shadows the surfaces defined by red lines in figure 5 (extend into the page) for designs 1,3 and 4, in order to reduce heat flux and carbon outflux from these side surfaces due to the finite radial component of the magnetic field vector. Depending on the magnetic field configuration of the tokamak, the particle flux vector incident on designs 3 and 4 (nose tiles) can have either a positive or negative radial component with respect to the major radius axis and so bi-directional radial shadowing of the probes is required; whereas the particle flux vector incident on design 1 (divertor target tiles) will always have a positive radial component and so uni-directional radial shadowing of the probes is sufficient.

Both designs 1 and 2 were installed on T5 at different sectors to investigate the dependence of ion gyroradius/probe length scale ( $r_g/l_p$ ) on the effective ion collection area of the probe, which satisfies  $A_{projected} \leq A_i \leq A_{physical}$ . The assumption that charged particles are collected over  $A_{projected}$ , rather than the physical area ( $A_{physical}$ ), is valid in the limit  $r_g/l_p \ll 1$ . The gyroradii of electrons and deuterium ions incident on T2 with 5 eV of energy, in the plane perpendicular to magnetic field, are  $r_{ge} = 0.008$  mm and  $r_{gi} = 0.5$  mm respectively, assuming  $B = 0.9$  T. The gyroradii of electrons and deuterium ions incident on T5 with 5 eV of energy are  $r_{ge} = 0.030$  mm and  $r_{gi} = 1.8$  mm respectively, assuming  $B = 0.25$  T. The ions incident on T5 have a gyroradius which is comparable to the probe dimensions (several millimeters). The radial shadowing feature was deemed non-essential for design 2 because tile heat flux is expected to be significantly reduced on T5.

All probes, except design 3 (N1 tile), receive particle flux from only a single toroidal direction. During conventional and Super-X divertor operation, where the outer strike point is on T2-T5, the collection area of the N1 probes is dominated by the surface defined by dimensions (c) and (h) rather than surface  $\hat{n}_{probe}$ ; see figure 6(bottom). The inner leg Super-X configuration<sup>18</sup> with the outer strike point on N1 would necessitate reversing the helicity of the magnetic field to ensure that the inner leg helicity matches the imbrication of the T2-T5 tiles. In this scenario, the particle flux incident on the N1 probes

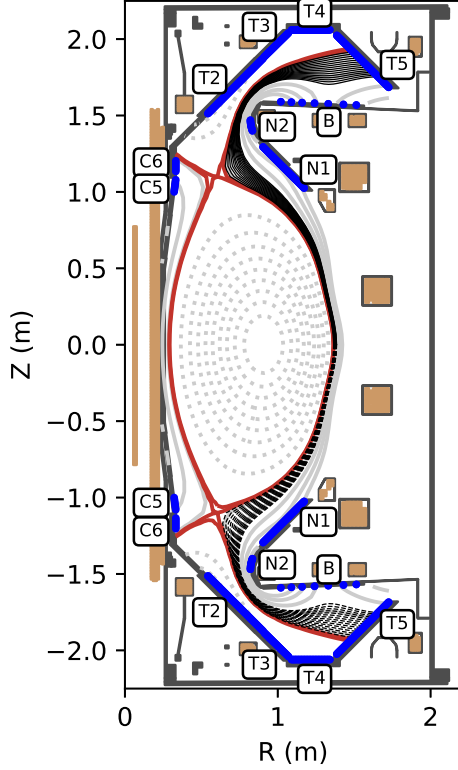


FIG. 4. Langmuir probe locations are shown in blue. Tile names are given: T2-T5 are target tiles; N1 and N2 are nose tiles, B are baffle tiles; C5 and C6 are centre column tiles. For illustration purpose a typical Super-X equilibrium is plotted (shot 45456, 0.445 s).

would be from the opposite toroidal direction and so the collection area would be determined by surface  $\hat{n}_{probe}$  instead.

The centre column probes have discrete tile penetrations to reduce tile stress, rather than a tile embedded cartridge containing multiple probes like the nose and target probe sets. Design 5 has an ellipse shape to reduce sharp edges on the probe and the tile cutout, where the incident field line angle on the centre column can be  $< 1^\circ$ . In addition, circular cut out holes were favorable for construction.

The baffle probes, design 6, also have discrete tile penetrations. These probes have a simple flush mounted circular design and monitor the ion flux to the baffle. The baffle tiles were not designed to act as a strike point target and so these probes are not expected to be used for detailed physics investigations.

The projected area of the probe along the magnetic field gives the lower bound for the effective collection area for both ions and electrons. As shown in figure 6, a portion of the recessed probe face is shadowed by the tile. The physical surface area of the unshadowed region is denoted by  $A_{unshadowed}$ . The projected area is:

Tile(s)	Sector	Divertor(s)	Design	# per set
T2-T4	4	L&U	1	101
T2-T4	10	L&U	1	101
T5	4	L	2	49
T5	4	U	1	49
T5	10	L	1	49
T5	10	U	2	49
N1	3	L&U	3	39
N1	9	L&U	3	39
N2	3	L&U	4	8
N2	9	L&U	4	8
C5,C6	4	L&U	5	17
B	4	L&U	6	7
B	10	L&U	6	7

TABLE I. Toroidal sector and upper(U)/lower(L) locations of the Langmuir probes. The MAST-U torus is split into 12 sectors. The probe designs are explained in section IV. # per set gives the number of probes per upper or lower divertor.

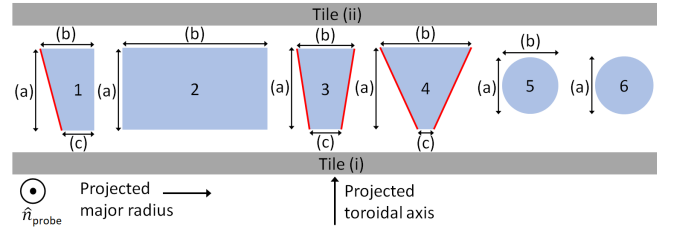


FIG. 5. The six probe designs. Each probe was rotated so that its surface-normal vector is perpendicular to the plane of the page. The major radius and toroidal axes were projected onto the plane of the page. Viewing the lower divertor from above. Dimensions are given in table II.

$$A_{projected} = A_{unshadowed} |\hat{n}_{probe} \cdot \hat{B}_{EFIT}|, \quad (2)$$

where  $\hat{n}_{probe}$  is the surface-normal unit vector of the probe.

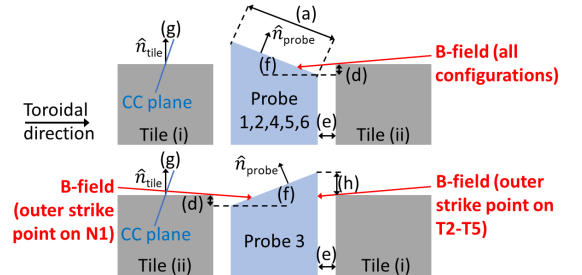


FIG. 6. Probe position relative to the tile. The Centre Column axis lies within the CC plane. Only probe 3 (N1 tile), shown at the bottom, is designed to handle particle flux from either toroidal direction. Tiles (i) and (ii) are consistent with the orientation shown in figure 5. Dimensions are given in table II.

Design	a	b	c	d	e	f [°]	g [°]	h
1 (PG)	5.08	3.34	2	0.200	1.0	10	0 or 0.781*	-
2 (PG)	5.08	9.00	-	0.200	1.0	10	0.781	-
3 (FGG)	5.01	3.60	2	0.300	1.0	3.5	0	3.75
4 (FGG)	5.08	5.66	1	0.377-0.713	1.0	10	0	-
5 (FGG)	3.53	3.50	-	0.224	0.5	7.3	0	-
6 (FGG)	3.60	-	-	0	0.5	0	0	-

TABLE II. Langmuir probe dimensions and probe material (PG=Pyrolytic Graphite and FGG=Fine Grain Graphite). Units are given in millimeters unless stated. \*0.781° is for T5 tile only. Dimension (h) is only relevant, in terms of calculating the probe collection area, for design 3.

	RG62	RG179
Impedance $Z$ ( $\Omega$ )	93	75
Inductance $L$ ( $\mu\text{H}/\text{m}$ )	0.411	0.360
Capacitance $C$ (pF/m)	47.6	64.0
Length (m)	19	18

TABLE III. Properties of RG62 and RG179 cables.

## V. DATA ANALYSIS

This section details the data analysis for calculating plasma parameters from multiplexer data collected during swept mode. There are four sections: V A explains how  $IV$  characteristics were generated from current and voltage waveforms, V B discusses the  $IV$  model and the fitting details, V C gives the formulae for plasma parameters, and V D lists additional assumptions.

### A. Generating $IV$ characteristics

#### 1. Cable capacitance, inductance and resistance

During the first and second MAST-U campaigns, the minimum time to sweep from the maximum to the minimum voltage was  $\geq 22 \mu\text{s}$ . Within this period the current and voltage measurements need to resolve the shape of the  $IV$  characteristic. The required frequency resolution is estimated to be an order of magnitude greater than the corresponding frequency for this time interval:  $f \sim 450 \text{ kHz}$  which is below the Nyquist frequency (500 kHz) of the system. The transition region of the  $IV$  characteristic ( $V_f \lesssim V < V_{plasma}$ , where  $V_{plasma}$  is the electric potential of the bulk plasma) has the greatest  $dI/dV$ , and hence the greatest  $dI/dt$  if  $dV/dt$  is constant. Figure 7(top) shows a typical voltage waveform. In the region -20 V to +20 V,  $dV/dt$  was reduced to both improve the voltage resolution of the transition region (determined empirically) and reduce the maximum  $dI/dt$  requirement.

Two types of radio frequency cable were used for the Langmuir probe system: (i) RG62 from the multiplexers to the marshalling cubicles; (ii) RG179 from the marshalling cubicles to the in-vessel probes. The cable properties are summarized in table III. The wavelength of a

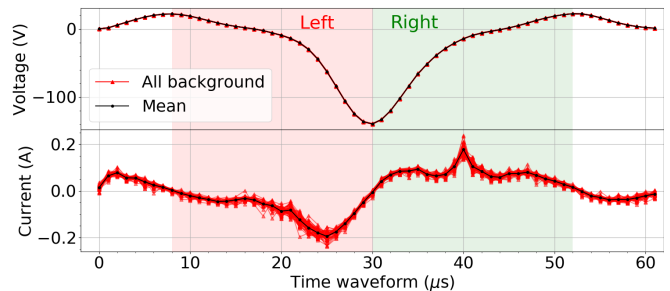


FIG. 7. Example of background waveforms from a single multiplexer channel acquired during  $-0.06 \leq t[\text{s}] \leq -0.01$  (no plasma). A total of 56 waveforms are plotted. Top shows the voltage waveform output from the multiplexer and bottom shows the measured current. The left and right voltage sweep periods are highlighted by shading.

signal of frequency  $f$  propagating inside a transmission line:

$$\lambda = \frac{1}{f(LC)^{1/2}}, \quad (3)$$

where  $C$  is the capacitance per unit length and  $L$  is the inductance per unit length. The wavelength of a 450 kHz signal in the RG62 and RG179 cables is 502 m and 463 m respectively, which is much longer than the cable lengths. Therefore, transmission line effects can be ignored and the capacitance and inductance from the cables can be modelled as lumped components. Using the data in table III, the effective capacitance and inductance due to the cabling is  $C_{par} \sim 2.1 \text{ nF}$  and  $L_{par} \sim 14.3 \mu\text{H}$  respectively. Maximum  $dV/dt$  is of the order of  $20 \text{ V}/\mu\text{s}$ , which gives an expected displacement current  $C_{par}dV/dt \sim 42 \text{ mA}$  based on cabling alone. Direct measurements of the displacement current are a factor of  $\sim 5$  greater as shown in figure 7(bottom); the experimentally determined parasitic capacitance is  $C_{par} \sim 10 \text{ nF}$ . Additional sources of capacitance include the multiplexer and amplifier system, the capacitance between the cable core and vacuum vessel feedthrough flange, and the capacitance between the probe and tile. The maximum  $dI/dt$  measured is of the order of  $0.1 \text{ A}/\mu\text{s}$ , which gives an expected voltage drop across the parasitic inductor  $L_{par}dI/dt \sim 1.43 \text{ V}$  based on cabling alone.

The resistance between the core and shield of the coaxial cable from the multiplexer to the vessel port and back is typically  $R_{par} \sim 12 \Omega$ . This provides an estimate of the parasitic resistance in the probe circuit. The voltage drop across the parasitic inductor and resistor results in overestimation of the  $IV$  characteristic width in the transition region, and hence electron temperature is overestimated. The mitigation of this effect is discussed in section V A 3.

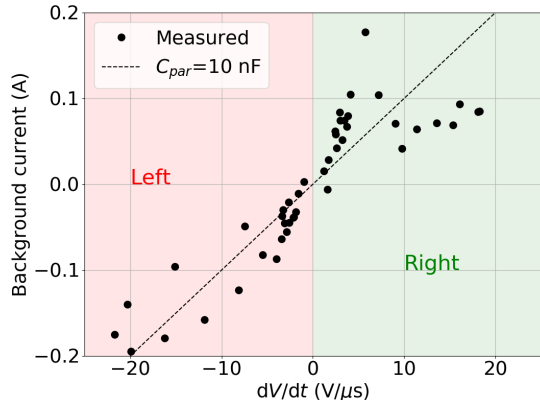


FIG. 8. Mean background current data from figure 7 plotted as a function of the rate of change of mean voltage. For comparison  $C_{par}dV/dt$  with  $C_{par} = 10$  nF is shown, but the measured data deviates from a linear relationship.

## 2. Removing displacement current

The current measured by the multiplexer ( $I_M$ ) has two contributions:

$$I_M = I_p + I_d, \quad (4)$$

where  $I_p$  is the conduction current from the plasma, and  $I_d$  is a displacement current which arises due to parasitic capacitance in the circuit and the fast voltage sweep rate ( $dV/dt \leq 20$  V/ $\mu$ s).

The current measured before the shot ( $t < 0$  s), when there is no plasma, is purely displacement current; this is referred to as the background current. Figure 7 shows the voltage and background current waveforms for a single multiplexer channel between  $-0.06 \leq t[s] \leq -0.01$ . The multiplexer was programmed to output a symmetric voltage waveform. The previous approach on MAST was to assume constant  $C_{par}$  and a displacement current of the form  $C_{par}dV/dt$ . The current measurements from symmetric left and right voltage sweeps were averaged to remove the displacement current contribution. This was not implemented on MAST-U data, however, due to the non-linear relationship between the background current and  $dV/dt$ , as shown in figure 8. Instead the mean background current for each channel, shown in figure 7(bottom) for one channel, was subtracted from all current waveforms to remove the displacement current contribution.

## 3. Averaging left and right symmetric sweeps

The error on the conduction current measurement has the following contributions: hardware noise, displacement current subtraction noise and plasma fluctuations

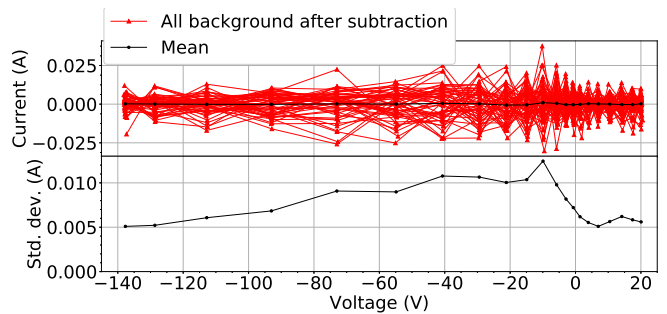


FIG. 9. Top shows background IV data after the mean background current was subtracted, and left and right sweeps were averaged. Bottom shows the corresponding standard deviation. Data are from figure 7.

over the voltage sweep period. The left and right sweep measurements of voltage ( $V_L, V_R$ ) and current ( $I_L, I_R$ ) were averaged to improve the signal to noise ratio by reducing random noise. Only data within the region between the two voltage maxima was analysed (e.g. the shaded regions between  $8 \leq t[\mu s] \leq 52$  in figure 7).

Figure 9(top) shows current measurements from  $-0.06 \leq t[s] \leq -0.01$  (no plasma) after the mean background current subtraction and subsequent averaging of the current and voltage data from the symmetric left and right voltage sweeps. Figure 9(bottom) shows the corresponding standard deviation; this is referred to as background noise, and it has contributions from hardware noise and displacement current subtraction noise. As expected the mean conduction current is  $\sim 0$  A, and the low standard deviation values ( $< 0.013$  A) demonstrate that the background current is highly reproducible. This justifies the subtraction approach outlined in section V A 2 for removing the displacement current contribution.

The averaging procedure also reduces the effect of the parasitic inductance as explained below. The output voltage from the multiplexer ( $V_M$ ) is distributed across three components:

$$V_M = V_{probe} + L_{par} \frac{dI_M}{dt} + R_{par} I_M, \quad (5)$$

where  $V_{probe}$  is the electric potential of the probe tip which needs to be determined in order to generate an IV characteristic. The mean of the multiplexer output voltages is:

$$\begin{aligned}
\bar{V}_M &= \frac{1}{2}(V_L + V_R) \\
&= \frac{1}{2} \underbrace{\left( V_{probe} \Big|_{V_M=V_L} + V_{probe} \Big|_{V_M=V_R} \right)}_{\bar{V}_{probe}} \\
&+ \frac{L_{par}}{2} \left( \frac{dI_M}{dt} \Big|_{V_M=V_L} + \frac{dI_M}{dt} \Big|_{V_M=V_R} \right) \\
&+ \frac{R_{par}}{2} \underbrace{\left( I_M \Big|_{V_M=V_L} + I_M \Big|_{V_M=V_R} \right)}_{R_{par} \bar{I}_M},
\end{aligned} \tag{6}$$

where  $\bar{V}_{probe}$  is the mean electric potential of the probe tip and  $\bar{I}_M$  is the mean current measured by the multiplexer.

An approximate equation for the mean voltage applied to the probe tip is:

$$\bar{V}_{probe} \approx \bar{V}_M - R_{par} \bar{I}_p, \tag{7}$$

where  $\bar{I}_p$  is the mean conduction current. In order to obtain a simple expression, it was assumed that there is no hysteresis in the  $I_d$  measurement (despite figure 8) and the non-linear dependence of  $I_p$  as a function of  $V_{probe}$  was neglected. Consequently the  $dI_M/dt$  terms cancel in equation 6 and  $\bar{I}_M \approx \bar{I}_p$ .

An estimate of the error on using equation 7 to calculate the mean probe voltage, due to the hysteresis in the  $I_d$  measurement, during the background period (when  $I_p = 0$ ) can be estimated using calculated values from figure 7: (i) assuming  $L_{par} = 6.5 \mu\text{H}$  and a maximum error term of the order of  $\sigma_L = (dI_d(V_L)/dt + dI_d(V_R)/dt)/2 \sim 0.05 \text{ A}\mu\text{s}^{-1}$  gives an error contribution of  $L_{par}\sigma_L = 0.325 \text{ V}$ ; (ii) assuming  $R_{par} = 12 \Omega$  and a maximum error term of the order of  $\sigma_R = (I_d(V_L) + I_d(V_R))/2 \sim 0.05 \text{ A}$  gives an error contribution of  $R_{par}\sigma_R = 0.6 \text{ V}$ . The total error of  $0.925 \text{ V}$  is insignificant compared to the total voltage sweep of the probe ( $160 \text{ V}$  in this example).

The greatest  $dI_p/dt$  is during the transition region of the  $IV$  characteristic which is dominated by electron current. Assuming a Boltzmann factor for the electron current, the mean conduction current in this region is:

$$\begin{aligned}
\bar{I}_p &= \frac{1}{2}(I_L + I_R) \\
&= \frac{I_{sat}^+}{2} \left[ \exp\left(\frac{V_{probe} \Big|_{V_M=V_L} - V_f}{T_e}\right) \right. \\
&\quad \left. + \exp\left(\frac{V_{probe} \Big|_{V_M=V_R} - V_f}{T_e}\right) \right].
\end{aligned} \tag{8}$$

The Taylor expansion of the exponential term about

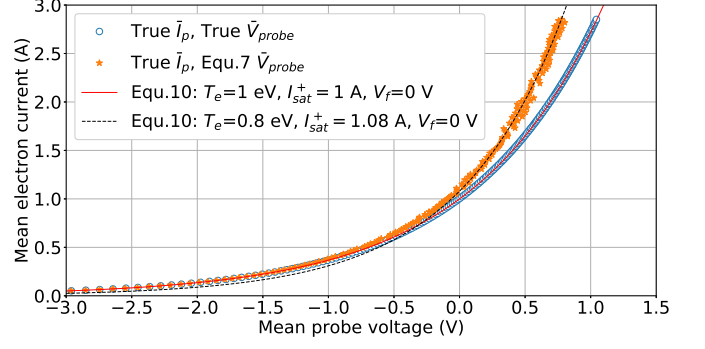


FIG. 10. Modelled mean electron current as a function of mean probe voltage. *True* refers to variables calculated numerically using equations 6 and 8; conditions were set to  $I_{sat}^+ = 1 \text{ A}$ ,  $T_e = 1 \text{ eV}$ ,  $V_f = 0 \text{ V}$ , maximum  $I_p = 3 \text{ A}$ , maximum  $dI_p/dt = 0.5 \text{ A}/\mu\text{s}$  from a linear voltage ramp,  $R_{par} = 12 \Omega$ ,  $L_{par} = 6.5 \mu\text{H}$ ,  $I_d = 0 \text{ A}$ . Two example curves from equation 10 are shown:  $T_e = 1 \text{ eV}$ ,  $I_{sat}^+ = 1 \text{ A}$ ,  $V_f = 0 \text{ V}$  has good agreement with the *True* data set; whereas  $T_e = 0.8 \text{ eV}$ ,  $I_{sat}^+ = 1.08 \text{ A}$ ,  $V_f = 0 \text{ V}$  has better agreement in the  $0 \leq \bar{V}_{probe} \leq 0.75 \text{ V}$  region with the data set that used equation 7 to calculate the mean probe voltage.

$V_{probe} = \bar{V}_{probe}$  to first order gives:

$$\begin{aligned}
\exp\left(\frac{V_{probe} - V_f}{T_e}\right) &= \exp\left(\frac{\bar{V}_{probe} - V_f}{T_e}\right) \\
&\times \left[ 1 + \frac{1}{T_e}(V_{probe} - \bar{V}_{probe}) + \dots \right].
\end{aligned} \tag{9}$$

Substituting equation 9 into equation 8:

$$\begin{aligned}
\bar{I}_p &= \frac{I_{sat}^+}{2} \exp\left(\frac{\bar{V}_{probe} - V_f}{T_e}\right) \\
&\times \left[ 2 + \frac{1}{T_e} \left( V_{probe} \Big|_{V_M=V_L} + V_{probe} \Big|_{V_M=V_R} - 2\bar{V}_{probe} \right) \right] \\
&= I_{sat}^+ \exp\left(\frac{\bar{V}_{probe} - V_f}{T_e}\right).
\end{aligned} \tag{10}$$

To first order the mean electron current measured by the multiplexer is equal to the electron current collected by the probe when it is at electric potential  $\bar{V}_{probe}$ . Including higher order terms would increase  $\bar{I}_p$  and the absolute error becomes more significant as  $dI_p/dt$  increases. For extreme conditions on MAST-U (described in the caption of figure 10), equations 6 and 8 were solved numerically to determine  $\bar{I}_p$  as a function of  $\bar{V}_{probe}$  (the *true* variables), and this had excellent agreement with the result from equation 10 (see blue dots and red solid line in figure 10); this justifies the approximation used in equation 9. The impact of neglecting the non-linear dependence of  $I_p$  in the calculation of the mean probe voltage was assessed by plotting *true*  $\bar{I}_p$  as a function of the approximate  $\bar{V}_{probe}$

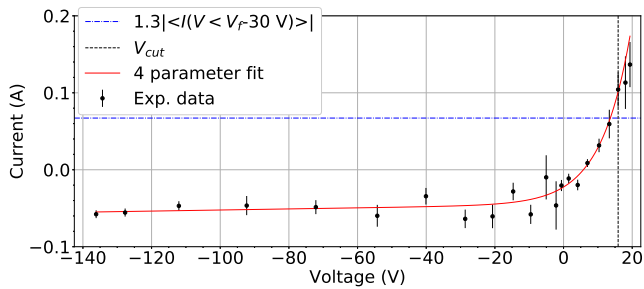


FIG. 11. Example  $IV$  characteristic from a divertor target probe (design 1) with the 4 parameter fit applied. The voltage waveform period was  $61 \mu\text{s}$ . Fitting parameters:  $T_e = 8.6 \pm 1.5$  eV,  $V_f = 5.8 \pm 0.6$  V,  $I_{sat}^+ = 45 \pm 7$  mA,  $\alpha = 0.069 \pm 0.086$  mA/V,  $\chi^2/\text{ndf} = 0.91$ . The upper cut off voltage ( $V_{cut}$ ) was defined by equation 12 with  $\beta = 1.3$ .

from equation 7;  $T_e$  can be underestimated by up to 20% depending on the analysis region (see orange stars and black dashed line in figure 10).

The error ( $\sigma$ ) associated with  $\bar{I}_p$  was taken as the population standard deviation of the two current measurements per voltage from the left and right sweeps. This error is dominated by the effect of changing plasma conditions during the voltage sweep. The minimum  $\bar{I}_p$  error for each voltage was set to the background noise.

## B. Interpretation of $IV$ data

A model is fit to the experimental  $IV$  data ( $\bar{I}_p$  as a function of  $\bar{V}_{probe}$ ) to extract plasma parameters. The standard model applied to MAST-U data during the first and second campaigns was a 4-parameter fit<sup>12</sup>, which was developed for unmagnetized conditions and takes into account non-saturation of the net ion current region due to sheath expansion:

$$I_{fit} = \begin{cases} I_{sat}^+ \left[ \exp\left(\frac{V-V_f}{T_e}\right) - 1 \right] & \text{if } V_f \leq V < V_{plasma} \\ I_{sat}^+ \left[ \exp\left(\frac{V-V_f}{T_e}\right) - 1 \right] - \alpha(V_f - V) & \text{if } V < V_f \end{cases} \quad (11)$$

where  $\alpha$  is the ion current per volt due to sheath expansion and the probe voltage must satisfy  $V < V_{plasma}$ , where  $V_{plasma}$  is the electric potential of the bulk plasma. The four fitting parameters are  $I_{sat}^+$ ,  $T_e$ ,  $V_f$  and  $\alpha$ . An example  $IV$  characteristic with the fit applied is shown in figure 11. Several assumptions must be satisfied for the model to be applicable for analysing  $IV$  data from magnetized conditions:

1. The ion saturation current is the ion current collected by the probe when the probe is biased  $V_f \leq V < V_{plasma}$ . The model assumes that sheath expansion is negligible for these probe voltages.

2. The collection area of the probe for each charged species to first order depends on  $r_g/l_p$ . As the probe voltage is swept ( $V < V_{plasma}$ ) different regions of the electron energy distribution function (EEDF) are sampled and so the mean gyro-radius for the collected electrons is a function of voltage. For electron energies 1 eV to 50 eV the gyroradius is 0.01 to 0.10 mm assuming  $B = 0.25$  T on T5. Therefore the strong magnetic field limit is satisfied ( $r_g/l_p \ll 1$ ) and so the electron collection area can be assumed constant and equal to the projected area ( $A_e = A_{projected}$ ). Since the electric field in the probe sheath repels electrons, the increased surface area of the sheath for  $V \ll V_{plasma}$  does not increase the magnitude of the electron current collected.

3. The return electrode in the circuit must have a sufficiently large collection area to prevent it from limiting the current collected by the probe<sup>5</sup>. The collection area of the return electrode is difficult to model without simulation or dedicated experiments<sup>22</sup> since it depends on parallel and cross-field transport rates. This assumption is more likely to be satisfied when the magnitude of the current collected by the probe is reduced and so this favours smaller probe sizes and restricting analysis to the region  $V \ll V_{plasma}$ .

4. The bulk plasma region adjacent to the probe sheath must not be perturbed when the probe voltage is swept. Probe experiments in tokamaks<sup>10,11</sup> have shown that a Langmuir probe is least perturbing when the probe voltage satisfies  $V \leq V_f$ . This region of the characteristic samples the high energy tail of the EEDF, and this group of electrons have a greater cross-field transport rate for repopulating drained flux tubes compared to the bulk of the distribution.

5. The standard approach for evaluating  $V_{plasma}$  is to locate the inflection point on the  $IV$  characteristic (e.g. zero crossing point of  $d^2I/dV^2$ ). In magnetized plasmas, however, the  $IV$  characteristic can be significantly distorted for  $V > V_f$  (see points 3 and 4 above in section VB) resulting in no clear inflection point or the inflection point location is no longer representative of  $V_{plasma}$ . Therefore,  $V_{plasma}$  was not evaluated directly from the  $IV$  characteristic. Equation 11 was fit to the  $IV$  data in the region  $V \leq V_{cut}$ , where  $V_{cut}$  is the upper cut-off voltage which is defined by equation 12. Note that  $V_{cut}$  is independent of  $V_{plasma}$  and it is assumed  $V_{cut} < V_{plasma}$ .

The above considerations necessitate applying the fit to the region  $V \leq V_f$  on the  $IV$  characteristic. In practice, however, a subset of the data from the region  $V > V_f$  must be included in the fit to ensure a satisfactory electron current to noise ratio to determine  $T_e$ , especially

when using short voltage sweep periods ( $< 100 \mu\text{s}$ ) which can limit the voltage resolution of the  $IV$  characteristic. The upper cut-off voltage was set to the first experimental data point that satisfies:

$$I(V = V_{cut}) \geq \beta | \langle I(V < V_f - 30 \text{ V}) \rangle |, \quad (12)$$

where  $V_{plasma} > V_{cut} \geq V_f$ ,  $\beta \geq 0$  is a constant which is specified as an input parameter in the analysis code, and  $| \langle I(V < V_f - 30 \text{ V}) \rangle |$  is an estimate of  $I_{sat}^+$  by calculating the mean of the measured current in the region  $V < V_f - 30 \text{ V}$ . The default value of  $\beta = 1.3$  was chosen to satisfy the following arbitrary expression:

$$\frac{V_{cut} - V_f}{V_{plasma} - V_f} = \frac{\ln(\beta + 1)}{\ln(I_{sat}^- / I_{sat}^+)} = 0.25, \quad (13)$$

where expressions for the ion ( $I_{sat}^+$ ) and electron ( $I_{sat}^-$ ) saturation currents are given by equations 18 and 29 respectively, and see section VD for assumptions regarding parameters in these expressions. The value  $\beta = 1.3$  results in a minimum kinetic energy of  $V_{plasma} - V_{cut} = 2.5T_e$  for an electron to be collected by the probe when it is biased at  $V = V_{cut}$ , assuming no energy loss mechanisms in the probe sheath. This corresponds to  $\sim 2.5\%$  of the electrons that travel into the probe sheath being collected by the probe (100% collected when  $V = V_{plasma}$ ), assuming a 3D Maxwellian velocity distribution and the collection depends only on the velocity component that is anti-parallel to the  $\hat{n}_{probe}$  direction. The electron temperature measurement is therefore sensitive to only the tail of the EEDF, and so the measurement would not be representative of the overall distribution in the case of a non-Maxwellian EEDF. Stangeby<sup>23</sup> has shown that for a bi-Maxwellian EEDF and analysing only  $V \leq V_f$ , a Langmuir probe measurement will yield the temperature corresponding to the hot population unless its relative density is extremely small. Langmuir probes, therefore, tend to overestimate  $T_e$  in magnetized plasmas<sup>7,23</sup>.

Curve fitting was implemented by minimising the following function:

$$\chi^2 = \sum_i^N \frac{(I_{fit}(V_i) - I(V_i))^2}{\sigma(V_i)^2}, \quad (14)$$

where  $N$  is the number of experimental data points included in the  $IV$  fit. Errors associated with fitting parameters were given by the diagonal elements of the covariance matrix. Assuming that the model equation is correct,  $\chi^2/\text{number of degrees of freedom}=1$  ( $\chi^2/\text{ndf}=1$ ) needs to be satisfied to ensure that the fitting parameter errors are scaled correctly. Figure 12 shows a histogram of  $\chi^2/\text{ndf}$  which contains data from 56583  $IV$  characteristics. In this example 65% of the fits satisfy  $\chi^2/\text{ndf} < 1$ . Fitting parameters errors are overestimated when  $\chi^2/\text{ndf} < 1$ , and so the majority of errors were conservative.

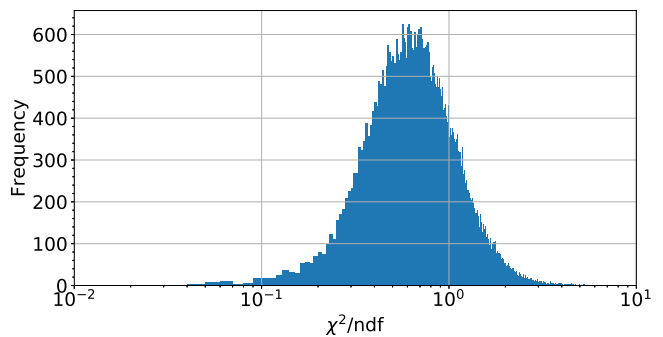


FIG. 12. Histogram of  $\chi^2/\text{number of degrees of freedom (ndf)}$  after applying the 4 parameter fit. The plot was generated using 56583  $IV$  characteristics from shot 46201. The mode and mean of the distribution are  $\sim 0.6$  and  $0.96$  respectively.

Figure 13 shows example  $I_{sat}^+$ ,  $T_e$ ,  $V_f$  and  $q_{\perp tile}$  (discussed in section VC3) profiles for a conventional divertor configuration in L-mode on MAST-U. The strike point position was held approximately constant during the measurement period (50 ms), and each probe took several measurements within this period. Cross-field transport of particles and energy from the midplane to the divertor causes non-exponential profiles of  $I_{sat}^+$ ,  $T_e$  and  $q_{\perp tile}$  at the divertor target<sup>24</sup>. The large scatter in the  $T_e$  and  $V_f$  data at  $R < 0.82 \text{ m}$  is due to the probe measuring a small current relative to the noise level: (i) the exponential function (determines  $T_e$  and  $V_f$ ), from equation 11, that is fit to the  $IV$  characteristic is highly sensitive to noise in the transition region; (ii) only a subset of the data in the transition region was included in the fit (determined by  $V_{cut}$ ) which exacerbates the noise problem.

### C. Calculating Plasma Parameters

This section explains how several additional parameters including total ion current to tiles, plasma density and heat flux are calculated from fitting parameters.

#### 1. Total Ion Current

The ion current density on a surface with its surface-normal vector parallel to the magnetic field is:

$$j_{\parallel B}^+ = \frac{I_{sat}^+}{A_i}, \quad (15)$$

where  $A_i$  is the effective collection area of the probe for ions. The ion current density on the tiles is:

$$j_{\perp tile}^+ = j_{\parallel B}^+ |\hat{n}_{tile} \cdot \hat{B}_{EFIT}|, \quad (16)$$

where  $\hat{n}_{tile}$  is the tile surface-normal unit vector and  $V_{plasma} > 0 \text{ V}$  is assumed. The total ion current on the

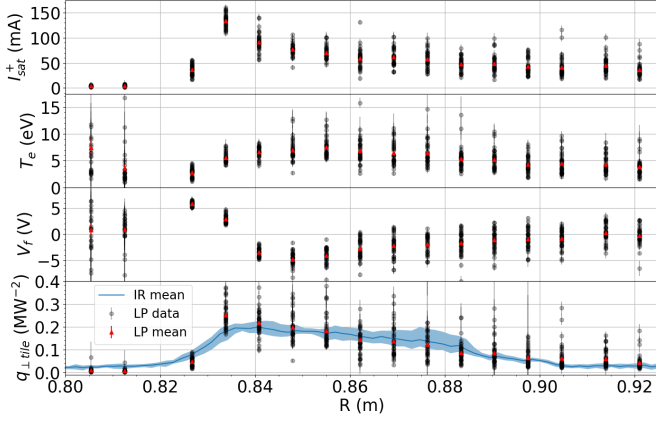


FIG. 13. Example ion saturation current ( $I_{sat}^+$ ), electron temperature ( $T_e$ ), floating potential ( $V_f$ ) and tile heat flux ( $q_{\perp tile}$ ) profiles at the outer divertor target (sector 4 lower) for a conventional magnetic equilibrium in L-mode. The data was acquired during the interval  $0.25 \leq t[s] \leq 0.3$  from shot 46201. Measurements from the Langmuir probe system are shown by black circles and the mean is shown by red triangles. Note that there are two dead probe channels at  $R \approx 0.82, 0.91$  m. The mean of the  $q_{\perp tile}$  measurements from IR thermography is shown by a blue line with the shaded region representing the range.

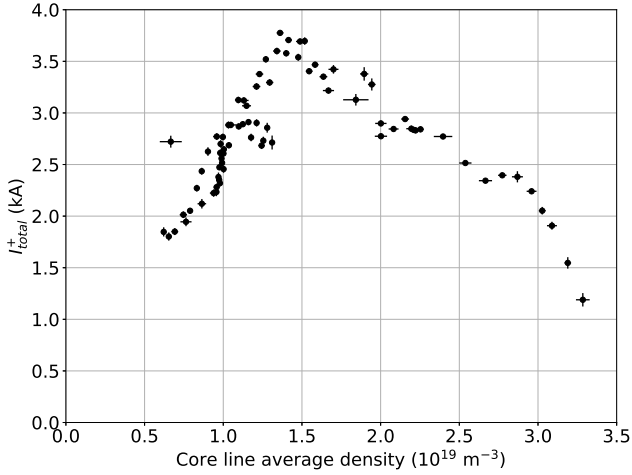


FIG. 14. Total ion current to the outer divertor target (sector 4 upper) as a function of core plasma density. Data from shots 45468, 45469, 45470 and 45473: ohmic heating only, plasma current 600 kA, double null, conventional divertor, L-mode.

tiles is calculated by integrating the  $j_{\perp tile}^+$  profile around the torus:

$$I_{total}^+ = \sum 2\pi R j_{\perp tile}^+ \Delta s, \quad (17)$$

where  $\Delta s$  is the poloidal distance between adjacent probes in the profile and  $R$  is major radius. Note that the integration should exclude the area on the tiles that

is shadowed by the toroidal inclination. This can be calculated experimentally (e.g. IR thermography analysis) or modelled using  $\hat{\mathbf{B}}_{EFIT}$ . Figure 14 shows an example rollover plot for a conventional divertor configuration on MAST-U:  $I_{total}^+$  as a function of the core line average plasma density. The transition from increasing ion target flux to decreasing is an indicator of detachment onset<sup>25</sup>.

## 2. Plasma density

An expression for the ion saturation current:

$$I_{sat}^+ = A_i e n_i \exp\left(\frac{-\epsilon_{pre}}{T_e}\right) c_s, \quad (18)$$

where  $n_i$  is the bulk plasma density;  $c_s$  is the ion sound speed:

$$c_s = \left(\frac{eT_e(1 + \gamma_C \epsilon_T)}{m_i}\right)^{1/2}, \quad (19)$$

where  $\gamma_C$  is the ion adiabatic index,  $\epsilon_T = T_i/T_e$ ;  $T_i$  is ion temperature and  $\epsilon_{pre}$  is the electric potential difference across the presheath:

$$\epsilon_{pre} \approx \frac{m_i c_s^2}{2e} - \frac{\epsilon_T T_e}{2}. \quad (20)$$

The plasma density is calculated by rearranging equation 18:

$$n_i = \frac{I_{sat}^+}{A_i e c_s} \exp\left(\frac{\epsilon_{pre}}{T_e}\right). \quad (21)$$

## 3. Heat Flux

There are three heat fluxes to consider: the heat flux received by the probe ( $q_{probe}$ ), the heat flux received by the tile ( $q_{\perp tile}$ ), and the heat flux received by an imaginary surface that has its surface-normal vector parallel to the magnetic field ( $q_{\parallel B}$ ). The latter is useful for comparing heat flux profiles when the magnetic field incidence angle on the tile varies, and for comparing heat flux decay lengths from the midplane and divertor target. The three equations are given below:

$$q_{\parallel B} = (\gamma T_e + E_{pot}) j_{\parallel B}^+, \quad (22)$$

$$q_{probe} = q_{\parallel B} |\hat{\mathbf{n}}_{probe} \cdot \hat{\mathbf{B}}_{EFIT}|, \quad (23)$$

$$q_{\perp tile} = q_{\parallel B} |\hat{\mathbf{n}}_{tile} \cdot \hat{\mathbf{B}}_{EFIT}| = (\gamma T_e + E_{pot}) j_{\perp tile}^+, \quad (24)$$

where  $E_{pot}$  is the potential energy released per incident ion, and  $\gamma$  is the sheath energy transmission coefficient which can be interpreted as the effective kinetic and thermal energy transferred to the surface, in units of  $T_e$ , per incident ion.

The  $\gamma$  term has electron ( $\gamma_e$ ) and ion ( $\gamma_i$ ) components:

$$\gamma = \gamma_i + \gamma_e. \quad (25)$$

The ion contribution is given by the sum of thermal energy and the kinetic energy gain from the electric potential difference from the bulk plasma to the surface<sup>25</sup>:

$$\gamma_i = (2T_e\epsilon_T + V_{plasma} - V_{tile})(1 - R_{iE})/T_e, \quad (26)$$

where  $R_{iE}$  is the ion kinetic energy reflection coefficient. The potential difference across the sheath region can be split into two components:

$$V_{plasma} - V_{tile} = (V_{plasma} - V_f) - (V_{tile} - V_f). \quad (27)$$

Equation 11 in the interval  $V_f \leq V < V_{plasma}$  can be rewritten as:

$$I = I_{sat}^- \exp\left(\frac{V - V_{plasma}}{T_e}\right) - I_{sat}^+, \quad (28)$$

where  $I_{sat}^-$  is the electron saturation current:

$$I_{sat}^- = \frac{en_i A_e}{4} \left(\frac{8eT_e}{\pi m_e}\right)^{1/2}. \quad (29)$$

Substituting  $V = V_f$  into equation 28 and rearranging gives the potential difference across the sheath region when the surface is floating:

$$V_{plasma} - V_f = T_e \ln\left(\frac{I_{sat}^-}{I_{sat}^+}\right). \quad (30)$$

Equation 30 allows calculation of  $V_{plasma}$ , and the equation can be directly substituted into equation 27.

Each electron incident on the surface contributes  $2T_e$  of thermal energy<sup>25</sup>:

$$\gamma_e = \frac{2A_i}{A_e} \exp\left(\frac{V_{tile} - V_f}{T_e}\right). \quad (31)$$

The exponential term accounts for the change in the collected electron current, from  $I_{sat}^+$ , when the surface is biased  $V \neq V_f$ .

The potential energy term has components from electron-ion recombination ( $\chi_{ei}$ ) and atom-atom recombination ( $\chi_{aa}$ ):

$$E_{pot} = \chi_{ei} + \chi_{aa}. \quad (32)$$

It is assumed that all deuterium ions recombine with electrons at the surface:

$$\chi_{ei} = 13.6 \text{ eV}. \quad (33)$$

The Frank-Condon dissociation energy per atom for the molecule  $D_2$  is 2.25 eV. A fraction  $R_{iN}$  of ions are reflected from the surface as neutrals before atom-atom recombination occurs. Therefore:

$$\chi_{aa} = 2.25(1 - R_{iN}) \text{ eV}. \quad (34)$$

Ions have normal-incidence on the probe surface after passing through the Debye sheath. Ion energy and particle reflection coefficients for deuterium ions incident on a carbon target are given by Eckstein<sup>26</sup>:

$$R_{iE} = \frac{0.05142\epsilon^{-0.2714}}{1 + 0.2668\epsilon^{1.316}}, \quad (35)$$

$$R_{iN} = \frac{0.1526\epsilon^{-0.2304}}{1 + 0.2113\epsilon^{1.287}}, \quad (36)$$

where

$$\epsilon = (2T_e\epsilon_T + V_{plasma} - V_{tile})/4.46507 \times 10^2. \quad (37)$$

The model used to calculate heat flux by Langmuir probes was validated by comparing  $q_{\perp tile}$  measurements with an independent diagnostic, IR thermography; see the bottom plot in figure 13. There is good agreement in terms of profile shape and magnitude. A detailed comparison study is planned to assess the agreement in a variety of plasma conditions (e.g. ohmic and beam heated, vary the detachment state of divertor, vary the divertor configuration) during power balance experiments.

#### D. Additional assumptions

The following assumptions are used by default in the analysis code:

1. Equation 31 assumes that the plasma potential satisfies  $V_{plasma} \geq V_{tile} = 0$  V.
2. An isothermal flow of ions in the probe sheath:  $\gamma_C = 1$ .
3. The ion mass was taken as the mass of a deuterium ion ( $m_i = 3.345 \times 10^{-27}$  kg). An effective ion mass could be used in the probe analysis if another diagnostic (e.g. spectroscopy) determined the relative abundance of ions.
4. The ion temperature is equal to the electron temperature ( $\epsilon_T = 1$ ). Retarding field analyser (RFA) measurements are planned for future MAST-U

campaigns to directly measure  $T_i$  in the divertor. Previous RFA measurements in the MAST divertor<sup>27</sup> were consistent with  $\epsilon_T \lesssim 1$  in L-mode plasmas, and  $\epsilon_T \gtrsim 1$  in both H-mode and additionally heated L-mode plasmas.

5. The effective collection areas for ions and electrons are both equal to the projected probe area along the magnetic field ( $A_i = A_e = A_{projected}$ ). This assumption will be explored in future work by comparing results from probe designs 1 and 2 on tile T5 (see section IV) in attached divertor conditions. Electron temperature measurements from the probes, which determine  $r_{ge}$  and  $r_{gi}$  (assuming  $\epsilon_T$  is known), are expected to be reliable in the attached regime<sup>8</sup>.
6. Secondary electron emission from the probe, due to incident ions and electrons, is neglected. Secondary electron emission yield is important for  $T_e \geq 30$  eV, but ion induced yields are insignificant for typical ion energies (of the order of 100 eV after acceleration in the probe sheath) at the target<sup>8,28</sup>.

## VI. SUMMARY

The Langmuir probe system on MAST-U features 850 probes which provide coverage of the centre column, divertor target and nose region; upper and lower divertors; and two toroidal locations per probe set. There are 40 bespoke electronic modules which have the total capability to drive and acquire data from 640 probes in each shot. There are two modes of operation: swept mode to acquire full  $IV$  characteristics for measurements of electron temperature, floating potential and ion saturation current ( $I_{sat}^+$ ); and  $I_{sat}^+$  mode to acquire ion current fluctuation statistics. The typical spatial and temporal resolutions of profiles are 1 cm in the poloidal plane and  $\sim 1$  ms. The default model to interpret the current-voltage characteristics is a four parameter fit which contains a linear model for the ion saturation region. To mitigate the effect of the magnetic field, analysis is restricted to the region of the  $IV$  characteristic that is sensitive to only the tail of the electron energy distribution function.

## ACKNOWLEDGMENTS

This work has been funded by the EPSRC Energy Programme [grant numbers EP/T012250/1 and EP/W006839/1]. To obtain further information on the data and models underlying this paper please contact PublicationsManager@ukaea.uk.

## AUTHOR DECLARATIONS

### Conflict of Interest

The authors have no conflicts to disclose.

## AUTHOR CONTRIBUTIONS

**P. J. Ryan:** Formal Analysis (lead); Investigation (lead); Writing - Original Draft Preparation (lead); Writing - Review & Editing (lead); Validation (equal). **S. D. Elmore:** Supervision (equal); Writing - Review & Editing (supporting). **J. R. Harrison:** Conceptualization (lead); Supervision (equal); Writing - Review & Editing (supporting). **J. Lovell:** Software (lead); Writing - Review & Editing (supporting); Validation (equal). **R. Stephen:** Resources (lead).

## DATA AVAILABILITY

Raw data were generated at MAST-U (UKAEA). Derived data supporting the findings of this study are available from the corresponding author upon reasonable request.

- <sup>1</sup>P. M. Valanju, M. Kotschenreuther, S. M. Mahajan, and J. Canik, “Super-X divertors and high power density fusion devices,” *Physics of Plasmas* **16**, 056110 (2009).
- <sup>2</sup>J. G. Clark, M. D. Bowden, and R. Scannell, “Low temperature Thomson scattering on MAST-U,” *Review of Scientific Instruments* **92**, 043545 (2021).
- <sup>3</sup>D. Bohm, E. H. Burhop, and H. S. Massey, *Characteristics of Electrical Discharges in Magnetic Fields*, edited by A. Guthrie and R. K. Wakerling (McGraw-Hill, New York, 1949) Chap. 2.
- <sup>4</sup>P. C. Stangeby, “Effect of bias on trapping probes and bolometers for Tokamak edge diagnosis,” *Journal of Physics D: Applied Physics* **15**, 1007 (1982).
- <sup>5</sup>M. Weinlich and A. Carlson, “Flush mounted Langmuir probes in an oblique magnetic field,” *Physics of Plasmas* **4**, 2151–2160 (1997).
- <sup>6</sup>F. Chen, *Introduction to Plasma Physics and Controlled Fusion*, 3rd ed. (Springer, Cham, CH, 2015) p. 161.
- <sup>7</sup>O. Février, C. Theiler, D. Oliveira, B. H., Labit, N. Fedorczak, and A. Baillod, “Analysis of wall-embedded Langmuir probe signals in different conditions on the Tokamak à Configuration Variable,” *Review of Scientific Instruments* **89**, 053502 (2018).
- <sup>8</sup>R. D. Monk, *Langmuir probe measurements in the divertor plasma of the JET tokamak*, Ph.D. thesis, University of London, London, UK (1996).
- <sup>9</sup>L. Rudischhauser, M. Endler, U. Höfel, K. C. Hammond, J. P. Kallmeyer, B. D. Blackwell, and Wendelstein 7-X Team, “The Langmuir probe system in the Wendelstein 7-X test divertor,” *Review of Scientific Instruments* **91**, 063505 (2020).
- <sup>10</sup>J. A. Tagle, P. C. Stangeby, and S. K. Erents, “Errors in measuring electron temperatures using a single Langmuir probe in a magnetic field,” *Plasma Physics and Controlled Fusion* **29**, 297 (1987).
- <sup>11</sup>P. C. Stangeby, “Determination of Te from a Langmuir probe in a magnetic field by directly measuring the probe’s sheath drop using a pin-plate probe,” *Plasma physics and controlled fusion* **37**, 1337 (1995).

- <sup>12</sup>J. P. Gunn, C. Boucher, B. L. Stansfield, and S. Savoie, “Flush-mounted probes in the divertor plates of Tokamak de Varennes,” *Review of scientific instruments* **66**, 154–159 (1995).
- <sup>13</sup>C. K. Tsui, J. A. Boedo, P. C. Stangeby, and T. Team, “Accounting for Debye sheath expansion for proud Langmuir probes in magnetic confinement fusion plasmas,” *Review of Scientific Instruments* **89**, 013505 (2018).
- <sup>14</sup>A. Bergmann, “Two-dimensional particle simulation of Langmuir probe sheaths with oblique magnetic field,” *Physics of Plasmas* **1**, 3598–3606 (1994).
- <sup>15</sup>A. Bergmann, “Two-dimensional particle simulation of the current flow to a flush-mounted Langmuir probe in a strong oblique magnetic field,” *Physics of Plasmas* **9**, 3413–3420 (2002).
- <sup>16</sup>J. Lovell, R. Stephen, S. Bray, G. Naylor, S. Elmore, H. Willett, M. Peterka, M. Dimitrova, A. Havranek, M. Hron, and R. Sharples, “A compact, smart Langmuir Probe control module for MAST-Upgrade,” *Journal of Instrumentation* **12**, C11008 (2017).
- <sup>17</sup>J. Lovell, *Development of Smart, Compact Fusion Diagnostics using Field-Programmable Gate Arrays*, Ph.D. thesis, Durham University, Durham, UK (2017).
- <sup>18</sup>W. Morris, J. R. Harrison, A. Kirk, B. Lipschultz, F. Militello, D. Moulton, and N. R. Walkden, “MAST upgrade divertor facility: a test bed for novel divertor solutions,” *IEEE Transactions on Plasma Science* **46**, 1217–1226 (2018).
- <sup>19</sup>W. Arter, V. Valeria, and G. Fishpool, “A CAD-based tool for calculating power deposition on tokamak plasma-facing components,” *IEEE Transactions on Plasma Science* **42**, 1932–1942 (2014).
- <sup>20</sup>L. Appel, G. Huysmans, L. Lao, P. McCarthy, D. Muir, E. Solano, J. Storrs, D. Taylor, and W. Zwingmann, “A unified approach to equilibrium reconstruction,” in *33rd EPS Conference on Plasma Physics* (Rome, 2006) p. 2.184.
- <sup>21</sup>J. Leland, S. Elmore, A. Kirk, H. J. van der Meiden, J. Scholten, S. Y. Allan, and J. W. Bradley, “Angular dependence measurements of Magnum-PSI plasmas using MAST-U angled-tip Langmuir probes,” *Nuclear Materials and Energy* **27**, 100954 (2021).
- <sup>22</sup>M. Weinlich, A. Carlson, V. Rohde, and K. Reinmüller, “Return currents from a single probe in a magnetized plasma,” *Contributions to Plasma Physics* **38**, 13–18 (1998).
- <sup>23</sup>P. C. Stangeby, “A problem in the interpretation of tokamak Langmuir probes when a fast electron component is present,” *Plasma Physics and Controlled Fusion* **37**, 1031 (1995).
- <sup>24</sup>T. Eich, B. Sieglin, A. Scarabosio, W. Fundamenski, R. J. Goldston, A. Herrmann, and A. U. Team, “Inter-ELM power decay length for JET and ASDEX Upgrade: measurement and comparison with heuristic drift-based model,” *Physical review letters* **107**, 215001 (2011).
- <sup>25</sup>P. Stangeby, *The Plasma Boundary of Magnetic Fusion Devices*, 1st ed. (Institute of Physics Publishing, Bristol, UK, 2000).
- <sup>26</sup>W. Eckstein, “Reflection (Backscattering),” Tech. Rep. (IPP 17/12, Garching: Max-Planck-Institut für Plasmaphysik, Germany, 2009).
- <sup>27</sup>S. Elmore, *Scrape-off layer ion temperature measurements on MAST by retarding field energy analyser*, Ph.D. thesis, University of Liverpool, Liverpool, UK (2013).
- <sup>28</sup>M. E. Woods, B. J. Hopkins, G. F. Matthews, G. M. McCracken, P. M. Sewell, and H. Fahrang, “An investigation of the secondary-electron emission of carbon samples exposed to a hydrogen plasma,” *Journal of Physics D: Applied Physics* **20**, 1136 (1987).